

Critical Role of the Exchange Interaction for the Electronic Structure and Charge-Density-Wave Formation in TiSe₂

Maria Hellgren,^{1,2} Jacopo Baima,¹ Raffaello Bianco,^{3,1} Matteo Calandra,¹ Francesco Mauri,^{3,4} and Ludger Wirtz⁵

¹*Institut de Minéralogie, de Physique des Matériaux et de Cosmochimie, Sorbonne Universités, Université Pierre et Marie Curie, CNRS, IRD, MNHN, 4 Place Jussieu, 75252 Paris, France*

²*Physics and Materials Science Research Unit, University of Luxembourg, 162a avenue de la Faïencerie, L-1511 Luxembourg, Luxembourg*

³*Dipartimento di Fisica, Università di Roma La Sapienza, Piazzale Aldo Moro 5, I-00185 Roma, Italy*

⁴*Graphene Labs, Fondazione Istituto Italiano di Tecnologia, Via Morego, I-16163 Genova, Italy*

⁵*Physics and Materials Science Research Unit, University of Luxembourg, 162a avenue de la Faïencerie, L-1511 Luxembourg, Luxembourg*

(Dated: October 19, 2017)

We show that the inclusion of screened exchange via hybrid functionals provides a unified description of the electronic and vibrational properties of TiSe₂. In contrast to local approximations in density functional theory, the explicit inclusion of exact, non-local exchange captures the effects of the electron-electron interaction needed to both separate the Ti-*d* states from the Se-*p* states and stabilize the charge-density-wave (CDW) (or low-T) phase through the formation of a *p* – *d* hybridized state. We further show that this leads to an enhanced electron-phonon coupling that can drive the transition even if a small gap opens in the high-T phase. Finally, we demonstrate that the hybrid functionals can generate a CDW phase where the electronic bands, the geometry, and the phonon frequencies are in agreement with experiments.

The charge density wave (CDW) instability is a common phenomenon in layered semi-metallic transition metal dichalcogenides (TMDs) [1] and has attracted considerable interest over the years, from both the experimental and the theoretical side. The CDW phase is often found to compete with superconductivity and thus plays a similar role as the anti-ferromagnetic phase in strongly correlated heavy fermion systems or in high-T_c cuprates [2–5]. This intriguing similarity has stimulated the search for a better understanding of the physical mechanism behind the CDW instability in TMDs [6].

The CDW instability in TiSe₂ is one of the most studied and debated. On the experimental side, neutron diffraction [7] and X-ray scattering [8] have established the existence of a commensurate 2 × 2 × 2 structural transition at 200 K. This is confirmed by angle resolved photo emission spectroscopy (ARPES) as well as by transport measurements [7], where an abrupt increase in resistivity is found at the same temperature. However, upon further cooling the resistivity reaches an anomalous maximum [7], after which a weak metallic behaviour is observed. By contrast, ARPES finds an insulating low-T phase, with a gap of approximately 0.15 eV [9–14]. In the high-T phase ARPES has not been able to conclude whether the system is semi-metallic or semi-conducting due to the very small indirect (possibly negative) gap. Theoretically, this fact makes TiSe₂ an ideal candidate to exhibit an excitonic insulator phase [9, 15–17] for which the CDW transition is driven by a purely electronic instability. Some recent experiments [18] partly support this scenario. On the other hand, excitonic correlations alone are insufficient as demonstrated in Ref. 19.

Additional experimental evidence for the CDW instability has been provided by vibrational spectra as a function of temperature. A complete softening of an optical phonon at the *L*-point has been observed in inelastic X-ray scattering experiments [20]. In Raman and infrared (IR) spectroscopy the transition is detected by the appearance of a large number of new modes [21, 22], some of which can be related to the CDW transition due to their strong temperature dependence.

On the theoretical side, density functional theory (DFT) within the standard local density approximation (LDA) or the semi-local PBE approximation predicts a structural instability at the correct wave vector [20, 23, 24] emphasising the role of the lattice distortion. However, orbital occupations obtained from the electronic band structure are in disagreement with ARPES measurements and CDW phonon frequencies strongly deviate from experiments. This suggests that a proper inclusion of exchange and correlations effects may be crucial to describe the CDW instability. It has been shown that the inclusion of nonlocal exchange already gives a much better description of the electronic bands in both the high- and low-T phase [13, 14, 25–27]. In Ref. 24 it was further shown that also the DFT+U approach improves the electronic band structure, bringing it into good agreement with ARPES spectra. This seeming improvement, however, was accompanied by a complete loss of the CDW instability.

In this work we provide a unified description of both the electronic band structure and the lattice dynamics of TiSe₂, and give a physical explanation for the CDW instability based on first-principle calculations. By an

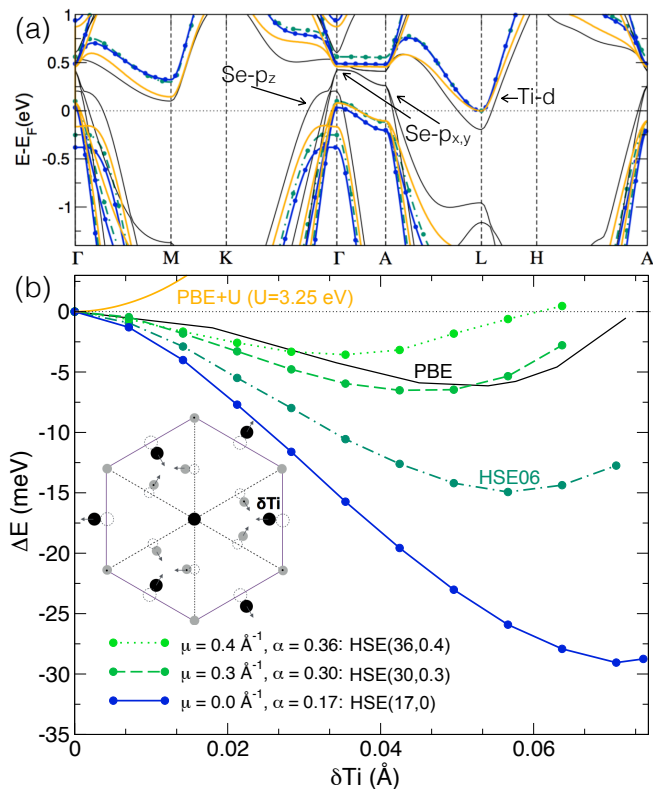


Figure 1. The upper panel (a) shows the band structure in the high-T phase in PBE (black solid line), HSE06 (green dash-dotted line and circles), HSE(17,0) (blue solid line and circles) and PBE+U ($U=3.5$ eV) (orange solid line). The lower panel (b) shows the corresponding energy gain as a function of δTi . We show also the corresponding results obtained by varying the α and μ parameters such that the band structure around conduction band minimum and valence band maximum is the same as the one of HSE06 and PBE+U.

inclusion of exact-exchange within the hybrid functionals we capture the strong Coulomb repulsion due to the localised Ti- d -states, thus correcting the orbital occupations. We also capture the long-range exchange interaction which enhances the electron-phonon coupling (EPC) and stabilizes the CDW phase through the formation of a Ti- d -Se- p hybridized state.

TiSe₂ is a layered material which in the high-T phase (>200 K) crystallises in the space group $P\bar{3}m1$. The CDW phase is characterised by a $2\times 2\times 2$ superstructure with a different space group $P\bar{3}c1$. The PBE phonon dispersion of the high-T phase was analysed in Refs. 23 and 24. The distortion pattern \mathbf{d}_{3L} (see Eq. 9 in Ref. 24) associated with the imaginary phonon frequencies at the three equivalent L points is of A_u symmetry and its projection on a single TiSe₂ layer is shown in the inset of Fig. 1(b). It is completely identified by its symmetry, the magnitude of the displacement δTi and the ratio $\delta\text{Ti}/\delta\text{Se}$. The layers are held together by van der Waals (vdW) forces and in the CDW phase adjacent layers are

rotated by 60 degrees. We verified that the vdW forces [28] do not play a role in the CDW distortion and by using the experimentally determined a and c lattice parameters [29], we indirectly account for the vdW contribution to the structure (see also Refs. [24, 30]). Although the spin-orbit coupling (SOC) splits the Se- p energy levels [26] it only gives a small contribution to the energetics [30]. Due to the increased computational cost we have therefore omitted SOC in the calculations presented here. Local functionals in DFT such as PBE give rise to an excess of electron occupation on the Ti- d -states compared to ARPES, mainly due to the large $p_z - d$ band overlap but also due to the overestimated $p_{x,y} - d$ band overlap (see black curve in Fig. 1 (a)). To cure this problem it is necessary to include the Coulomb repulsion or 'U' due to the localised Ti- d states. A simple corrective procedure to incorporate this effect is the DFT+U approach [31]. Indeed, in Ref. 24 it was shown that the $p - d$ band overlap reduced significantly (see orange curve Fig. 1 (a)). However, it was also found that the energy gain in the distortion decreases by increasing 'U' [30]. The hybrid functionals contain a fraction of exact-exchange and therefore naturally incorporate the repulsive 'U' interaction [32]. In addition, they exhibit the long-range exchange interaction, which generates the attractive electron-hole interaction at the linear response level [33, 34]. The description of screening is rather simplified using a pre-factor α and a range-separated Coulomb potential defined by μ . These parameters can be fitted in various ways but often the HSE06 parameters ($\alpha = 0.25, \mu = 0.2 \text{ \AA}^{-1}$) give good results [35]. In this work we have used the freedom of varying (α, μ) to reveal the critical role played by exchange, and to shed light on the mechanism that drives the CDW transition in TiSe₂.

In Fig. 1 (a) we plot the results for the band structure in the high-T phase with PBE, PBE+U and HSE06 [30, 37–41]. In Fig. 1 (b) we plot the corresponding energy gain as a function of δTi by displacing the atoms according to the \mathbf{d}_{3L} CDW pattern (using the experimentally determined ratio $\delta\text{Ti}/\delta\text{Se} = 3$ [7]). We found HSE06 to give an enhanced negative curvature and energy gain of approximately a factor of 2 compared to PBE. This difference is mainly attributed to an overscreening at the PBE level, i.e., due to the overestimation of the metallicity of the system. However, this is not the complete picture. We see that PBE+U and HSE06 have almost identical orbital occupations and gaps - both in rather good agreement with experiment [13, 14, 30] - but in PBE+U the instability is absent. This suggests that the long-range (or nonlocal) Coulomb exchange interaction is important for the formation of the CDW phase, as demonstrated explicitly in Figure 1 (b). We have calculated the energy gain using a set of (α, μ) parameters all tuned to give similar band-structures to HSE06 and PBE+U. By reducing the range, i.e., by increasing μ , thus approaching the PBE+U limit, the instability quickly vanishes (green

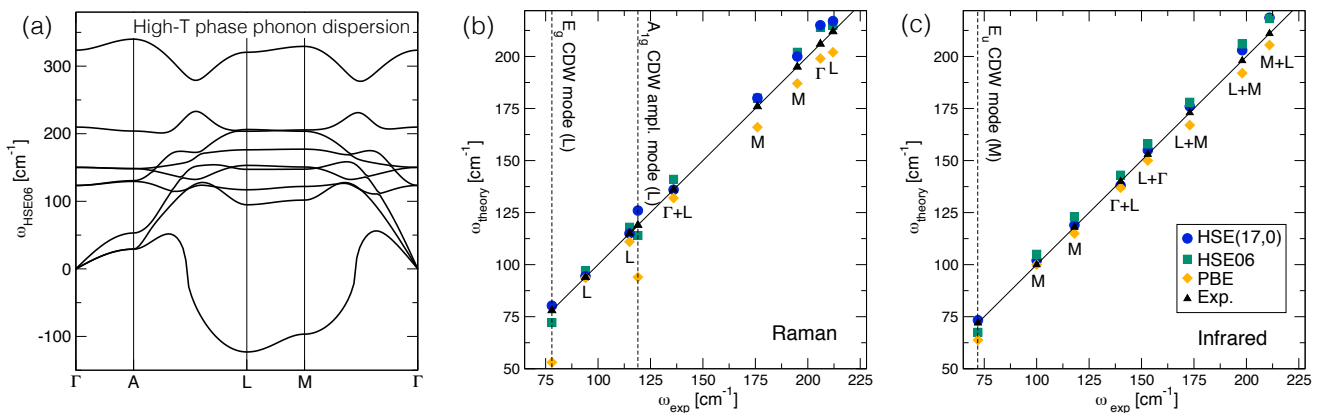


Figure 2. (a) Phonon dispersion of the high-T phase (HSE06). (b-c) Experimental [21, 36] versus calculated phonon frequencies of Raman and IR modes in the low-T phase. Modes related to the CDW distortion are marked by vertical dashed lines. The labels refer to the largest components of the phonon eigenvector with respect to the eigenvectors of the high-T structure.

curves). Instead, with an infinite range (HSE(17,0)) the energy gain increases substantially as does the amplitude of the distortion. After relaxing the atomic positions in the CDW phase, we find $\delta\text{Ti} = 0.055, 0.061, 0.082 \text{ \AA}$ with PBE, HSE06 and HSE(17,0) respectively. In experiment, $\delta\text{Ti} = 0.085 \pm 0.014 \text{ \AA}$ [7], thus suggesting a long-range (or unscreened) Coulomb interaction. Based on the above analysis, we will continue to discuss the mechanism for the CDW transition, but first we analyze the properties of the CDW phase.

The electronic band structure in comparison with ARPES suggests that the CDW phase is accurately captured with hybrid functionals [14, 30]. However, as seen above, a good description of the band structure alone is insufficient. The vibrational frequencies are proportional to the second derivative of the energy and thus provide an additional stringent test for the validity of different approximations. We have calculated the harmonic Raman and IR active phonon frequencies in the CDW phase within both HSE06 and the infinite range HSE(17,0) using a finite difference approach as implemented in the CRYSTAL code [42].

In Fig. 2 we compare the theoretical frequencies with low-T experimental Raman [36] and IR [21] frequencies (at 11 K and 20 K, respectively). We analyze the spectra of the CDW phase by back-folding of the phonons at A , L and M of the high-T phase Brillouin zone (see HSE06 phonon dispersion [43] in Fig. 2 (a)) onto the Γ point of the low-T phase Brillouin zone [30]. In the following, the high-symmetry points of the $2 \times 2 \times 2$ supercell are marked with a bar. For all three approximations, we find an overall good agreement with the experimental results [21, 36, 44–47]. However, there are three notable exceptions of particular interest for this work: these are the modes related to the instabilities of the high-T structure (marked by vertical dashed lines). The three-fold degenerate imaginary phonon frequency at L splits into one

A_{1g} and a two-fold degenerate E_g mode, which are both Raman active. These have been previously identified as being related to the CDW transition from their experimental temperature dependence [21, 22]. In fact, the A_{1g} (amplitude) mode corresponds to the oscillations of the CDW order parameter. The imaginary phonon frequency at M similarly gives rise to an E_u IR active phonon and to one A_{1u} inactive mode. The frequencies of the CDW modes are systematically underestimated by PBE (20% and 30% for the A_{1g} and E_g modes, respectively). HSE06 brings these frequencies in much better agreement with experiment (now underestimated by 4% and 7%, respectively). HSE(17,0), which gave the best geometry, also gives excellent CDW mode frequencies (overestimated by 5% and 2%, respectively). Since the frequencies of these modes depend very sensitively on the CDW potential energy surface (compare Fig. 1 (b)), they represent an important confirmation that the hybrid functionals reliably reproduce the electronic structure of TiSe_2 .

With a reliable description of the vibrational and electronic properties, we can now analyze in detail the physical mechanism that is responsible for the CDW instability in TiSe_2 . Figure 3 (a) shows the HSE06 band structure in both the low-T and high-T phase (the latter one is back-folded into the Brillouin zone that corresponds to the $2 \times 2 \times 2$ supercell of the low-T phase). At the CDW distortion, the three-fold degenerate Ti- d band splits into a band with dominant d_{z^2} character derived from the Ti atom in the supercell that does not move with the distortion, and a two-fold degenerate band with Ti- d and Se- p hybridization in a small region around $\bar{\Gamma}$ due to the interaction between the p and d states. Similarly, the Se- p bands move to lower energy and hybridize with Ti- d states around $\bar{\Gamma}$. Such $p-d$ hybridization, discussed also in Refs. 11, 48, and 49, is observed by studying the site-projected orbitals onto spherical harmonics before and after the transition. Panel (b) presents a zoom

of the region around $\bar{\Gamma}$, showing the effect of a small \mathbf{d}_{3L} distortion on the electronic structure. We see that the distortion only changes the $p-d$ gap while leaving the rest of the electronic structure almost unaffected. We can therefore assume that it is mainly the $p-d$ states around $\bar{\Gamma}$ which are involved in the transition and extract the EPC, or, more precisely, the deformation potential \mathcal{D} for the different approximations. The deformation potential is defined as $\mathcal{D} = \langle \bar{\Gamma}d | \delta V / \delta d_{3L} | \bar{\Gamma}p \rangle$, where the variation of the total self-consistent potential V is taken with respect to the magnitude d_{3L} of the \mathbf{d}_{3L} distortion. The states $|\bar{\Gamma}d\rangle$ and $|\bar{\Gamma}p\rangle$ with energy difference \mathcal{E}_0 are obtained from the Ti- d and Se- p states at L and Γ in the undistorted unit cell by back-folding them onto $\bar{\Gamma}$ in the supercell. Without loss of generality, all quantities can be taken as real in the supercell. The p and d states are superimposed and illustrated in Fig. 3 (c) together with the $p-d$ hybridized state in the CDW phase. We also note from first order perturbation theory that $\mathcal{D} = \langle \delta(\bar{\Gamma}d) / \delta d_{3L} | \bar{\Gamma}p \rangle \times \mathcal{E}_0$ and hence (at fixed \mathcal{E}_0) \mathcal{D} measures the overlap between the variation of the d state with the distortion and the undistorted p state. We then obtain \mathcal{D} using a finite difference approach [50]. At small but finite d_{3L} we construct the 2×2 submatrix of the Hamiltonian \mathcal{H} : $\mathcal{H}_{dd} = -\mathcal{E}_0/2 + \mathcal{O}(d_{3L}^2)$, $\mathcal{H}_{pp} = \mathcal{E}_0/2 + \mathcal{O}(d_{3L}^2)$ and $\mathcal{H}_{pd} = \mathcal{H}_{dp} = \mathcal{D}d_{3L} + \mathcal{O}(d_{3L}^2)$ and diagonalize it to obtain $\mathcal{D}^2 = \frac{1}{4}(\mathcal{E}^2 - \mathcal{E}_0^2)/d_{3L}^2$, where \mathcal{E} is the $p-d$ gap upon the distortion and we have discarded the higher order terms in d_{3L} . The results obtained from this procedure can be found in Fig. 3 (d). Although some coupling already exists between p and d states at the PBE level, the deformation potential (and so the EPC) is strongly enhanced via the nonlocal exchange potential in V provided by the inclusion of long-range exchange. Indeed, a comparison between PBE and PBE+U shows that U has no effect on the EPC. For the approximations with the same band structure we see the same trend in Figs. 1 (b) and 3 (d) and hence we conclude that it is the nonlocal exchange interaction that determines the strength of the instability. The inclusion of SOC splits and slightly changes the dispersion of the Se- p bands close to the Fermi level but has only a small quantitative effect on the EPC [30, 51]. Our result goes in line with some previous findings that the EPC can be strongly enhanced by nonlocal exchange, notably in weakly doped 2D materials [50, 53–55] and some high- T_c superconductors [56]. Although the band structure in HSE06, which we used as a reference, has a small negative $p-d$ gap (-0.1 eV) in the high-T phase, the instability does not crucially depend on the existence of a Fermi surface. In fact, due to the enhanced EPC, the CDW phase can exist even if the gap in the high-T phase is positive. This is easily demonstrated by increasing the amount of exact-exchange (α). With $\mu = 0.2 \text{ \AA}^{-1}$ fixed, the instability persists up to $\alpha = 0.35$ when the gap is as large as 0.2 eV. At larger values of the gap (or α) the hybridiza-

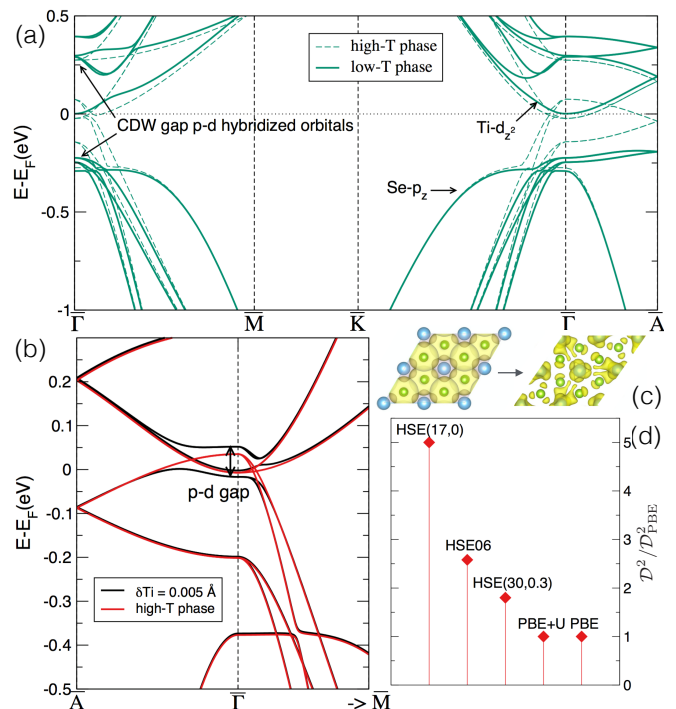


Figure 3. (a) HSE06 band-structure of undistorted (high-T) and CDW (low-T) phases of TiSe_2 . Panel (b) shows a zoom around the Fermi level and the EPC between the $p-d$ states is calculated in panel (d)). The value for $\mathcal{D}_{\text{PBE}}^2 = 8 \text{ eV}^2 / \text{\AA}^2$ (where d_{3L} is measured in units of $\delta\text{Ti} / \delta\text{Se} = 3$). Panel (c) demonstrates the mixing (hybridization) of these orbitals [52] in the CDW phase.

tion of Ti- d -and Se- $p_{x,y}$ bands is suppressed and the instability disappears. If we instead decrease $\alpha < 0.25$ the energy gain reaches a maximum around $\alpha = 0.15$. At smaller values of α the CDW phase becomes metallic and the energy gain drops. This unusual behaviour as a function of α (or the gap) shares some features with the excitonic insulator transition (EIT) of Kohn et al.[15, 57]. The EIT arises in a two band model (similar to the p and d bands in TiSe_2) when tuned until the value of the $p-d$ gap is smaller than the exciton binding energy. As a result, p and d orbitals mix and form a new ground state with lower symmetry. Since the symmetry of the lattice is kept fixed, the EIT is a purely electronic effect. In our calculations it was not possible to generate a symmetry lowering of the electronic density alone. The mechanism that we found relies on the simultaneous lattice distortion and strong EPC, enhanced by the exchange interaction. Whether the system is still influenced by excitonic effects can be determined by studying the excitation spectrum, but this we leave for future work.

M.H. and L.W. gratefully acknowledge financial support from the FNR (projects RPA-phonon and INTER/ANR/13/20/NANOTMD). The authors acknowledge support from the European Union Horizon 2020

research and innovation programme under Grant agreement No. 696656-GrapheneCore1. and by Agence Nationale de la Recherche under the reference n. ANR-13-IS10-0003-01 and by Prace. Calculations were performed at IDRIS, CINES, CEA and BSC TGCC. The authors are grateful to K. Rossnagel, for having supplied to them the image data of ARPES experiment.

-
- [1] J. A. Wilson, F. J. D. Salvo, and S. Mahajan, *Advances in Physics* **24**, 117 (1975).
- [2] S. Y. Li, G. Wu, X. H. Chen, and L. Taillefer, *Phys. Rev. Lett.* **99**, 107001 (2007).
- [3] A. F. Kusmartseva, B. Sipos, H. Berger, L. Forró, and E. Tutiš, *Phys. Rev. Lett.* **103**, 236401 (2009).
- [4] E. Morosan, H. W. Zandbergen, B. S. Dennis, J. W. G. Bos, Y. Onose, T. Klimczuk, A. P. Ramirez, N. P. Ong, and R. J. Cava, *Nat Phys* **2**, 544 (2006).
- [5] D. Qian, D. Hsieh, L. Wray, E. Morosan, N. L. Wang, Y. Xia, R. J. Cava, and M. Z. Hasan, *Phys. Rev. Lett.* **98**, 117007 (2007).
- [6] K. Rossnagel, *J. Phys.: Condens. Matter* **23**, 213001 (2011).
- [7] F. J. Di Salvo, D. E. Moncton, and J. V. Waszczak, *Phys. Rev. B* **14**, 4321 (1976).
- [8] Y. I. Joe, X. M. Chen, P. Ghaemi, K. D. Finkelstein, G. A. de la Pena, Y. Gan, J. C. T. Lee, S. Yuan, J. Geck, G. J. MacDougall, T. C. Chiang, S. L. Cooper, E. Fradkin, and P. Abbamonte, *Nat Phys* **10**, 421 (2014).
- [9] T. Pillo, J. Hayoz, H. Berger, F. Lévy, L. Schlapbach, and P. Aebi, *Phys. Rev. B* **61**, 16213 (2000).
- [10] T. E. Kidd, T. Miller, M. Y. Chou, and T.-C. Chiang, *Phys. Rev. Lett.* **88**, 226402 (2002).
- [11] K. Rossnagel, L. Kipp, and M. Skibowski, *Phys. Rev. B* **65**, 235101 (2002).
- [12] H. Cercellier, C. Monney, F. Clerc, C. Battaglia, L. Despont, M. G. Garnier, H. Beck, P. Aebi, L. Patthey, H. Berger, and L. Forró, *Phys. Rev. Lett.* **99**, 146403 (2007).
- [13] P. Chen, Y. H. Chan, X. Y. Fang, Y. Zhang, M. Y. Chou, S. K. Mo, Z. Hussain, A. V. Fedorov, and T. C. Chiang, *Nature Commun.* **6**, 8943 (2015).
- [14] Y.-H. P. Chen, X. Chan, S. Fang, Z. Mo, Z. Hussain, A. V. Fedorov, M. Chou, and T. C. Chiang, *Scientific Reports* **6**, 37910 (2016).
- [15] D. Jérôme, T. M. Rice, and W. Kohn, *Phys. Rev.* **158**, 462 (1967).
- [16] C. Monney, H. Cercellier, F. Clerc, C. Battaglia, E. F. Schwier, C. Didiot, M. G. Garnier, H. Beck, P. Aebi, H. Berger, L. Forró, and L. Patthey, *Phys. Rev. B* **79**, 045116 (2009).
- [17] C. Monney, C. Battaglia, H. Cercellier, P. Aebi, and H. Beck, *Phys. Rev. Lett.* **106**, 106404 (2011).
- [18] T. Rohwer, S. Hellmann, M. Wiesenmayer, C. Sohrt, A. Stange, B. Slomski, A. Carr, Y. Liu, L. M. Avila, M. Kallane, S. Mathias, L. Kipp, K. Rossnagel, and M. Bauer, *Nature* **471**, 490 (2011).
- [19] M. Porer, U. Leierseder, J. M. Ménard, H. Dachraoui, L. Mouchliadis, I. E. Perakis, U. Heinzmann, J. Demsar, K. Rossnagel, and R. Huber, *Nat Mater* **13**, 857 (2014).
- [20] F. Weber, S. Rosenkranz, J.-P. Castellán, R. Osborn, G. Karapetrov, R. Hott, R. Heid, K.-P. Bohnen, and A. Alatas, *Phys. Rev. Lett.* **107**, 266401 (2011).
- [21] J. A. Holy, K. C. Woo, M. V. Klein, and F. C. Brown, *Phys. Rev. B* **16**, 3628 (1977).
- [22] C. S. Snow, J. F. Karpus, S. L. Cooper, T. E. Kidd, and T.-C. Chiang, *Phys. Rev. Lett.* **91**, 136402 (2003).
- [23] M. Calandra and F. Mauri, *Phys. Rev. Lett.* **106**, 196406 (2011).
- [24] R. Bianco, M. Calandra, and F. Mauri, *Phys. Rev. B* **92**, 094107 (2015).
- [25] M. Cazzaniga, H. Cercellier, M. Holzmann, C. Monney, P. Aebi, G. Onida, and V. Olevano, *Phys. Rev. B* **85**, 195111 (2012).
- [26] Z. Vydrova, E. F. Schwier, G. Monney, T. Jaouen, E. Razzoli, C. Monney, B. Hildebrand, C. Didiot, H. Berger, T. Schmitt, V. N. Strocov, F. Vanini, and P. Aebi, *Phys. Rev. B* **91**, 235129 (2015).
- [27] Z. Zhu, Y. Cheng, and U. Schwingenschlögl, *Phys. Rev. B* **85**, 245133 (2012).
- [28] S. Grimme, *Journal of Computational Chemistry* **27**, 1787 (2006).
- [29] C. Riekel, *Journal of Solid State Chemistry* **17**, 389 (1976).
- [30] See Supplemental Material for further details.
- [31] V. I. Anisimov, J. Zaanen, and O. K. Andersen, *Phys. Rev. B* **44**, 943 (1991).
- [32] B. Himmetoglu, A. Floris, S. de Gironcoli, and M. Cococcioni, *International Journal of Quantum Chemistry* **114**, 14 (2014).
- [33] J. Paier, M. Marsman, and G. Kresse, *Phys. Rev. B* **78**, 121201 (2008).
- [34] A.-M. Ferrari, R. Orlando, and M. Rerat, *J. Chem. Theory and Comput.* **11**, 3245 (2015).
- [35] J. Heyd, G. E. Scuseria, and M. Ernzerhof, *The Journal of Chemical Physics* **118**, 8207 (2003).
- [36] S. Sugai, K. Murase, S. Uchida, and S. Tanaka, *Solid State Communications* **35**, 433 (1980).
- [37] P. Giannozzi *et al.*, *J. Phys.: Condens. Matter* **21**, 395502 (2009).
- [38] R. Dovesi, R. Orlando, A. Erba, C. M. Zicovich-Wilson, B. Civalleri, S. Casassa, L. Maschio, M. Ferrabone, M. D. L. Pierre, P. Darco, Y. Noel, M. Causa, M. Rerat, and B. Kirtman, *Int. J. Quantum Chem.* **114**, 1287 (2014).
- [39] G. Kresse and J. Furthmüller, *Phys. Rev. B* **54**, 11169 (1996).
- [40] G. Kresse and J. Furthmüller, *Comput. Mater. Sci.* **6**, 15 (1996).
- [41] G. Kresse and D. Joubert, *Phys. Rev. B* **59**, 1758 (1999).
- [42] F. Pascale, C. Zicovich-Wilson, F. Lopez, B. Civalleri, R. Orlando, and R. Dovesi, *J. Comput. Chem.* **25**, 888 (2004).
- [43] The phonon dispersion is approximated on a $2 \times 2 \times 2$ q-grid.
- [44] S. Uchida and S. Sugai, *Physica B+C* **105**, 393 (1981).
- [45] W. Y. Liang, G. Lucovsky, J. C. Mikkelsen, and R. H. Friend, *Philosophical Magazine Part B* **39**, 133 (1979).
- [46] J. A. Wilson, *physica status solidi (b)* **86**, 11 (1978).
- [47] D. L. Duong, G. Ryu, A. Hoyer, C. Lin, M. Burghard, and K. Kern, *ACS Nano* **11**, 1034 (2017).
- [48] N. G. Stoffel, S. D. Kevan, and N. V. Smith, *Phys. Rev. B* **31**, 8049 (1985).
- [49] J. van Wezel, P. Nahai-Williamson, and S. S. Saxena,

- Phys. Rev. B **81**, 165109 (2010).
- [50] M. Lazzeri, C. Attacalite, L. Wirtz, and F. Mauri, Phys. Rev. B **78**, 081406 (2008).
 - [51] M. J. Verstraete, M. Torrent, F. Jollet, G. Zérah, and X. Gonze, Phys. Rev. B **78**, 045119 (2008).
 - [52] The iso-surface of the square of the Bloch orbitals were obtained within HSE06 using VASP and VESTA (K. Momma and F. Izumi, J. Appl. Crystallogr., *44*, 1272 (2011)).
 - [53] C. Attacalite, L. Wirtz, M. Lazzeri, F. Mauri, and A. Rubio, Nano Letters **10**, 1172 (2010).
 - [54] M. Calandra, P. Zocante, and F. Mauri, Phys. Rev. Lett. **114**, 077001 (2015).
 - [55] B. Pamuk, J. Baima, R. Dovesi, M. Calandra, and F. Mauri, Phys. Rev. B **94**, 035101 (2016).
 - [56] Z. P. Yin, A. Kutepov, and G. Kotliar, Phys. Rev. X **3**, 021011 (2013).
 - [57] W. Kohn, Phys. Rev. Lett. **19**, 439 (1967).

**SUPPLEMENTAL MATERIAL FOR:
CRITICAL ROLE OF THE EXCHANGE INTERACTION FOR THE ELECTRONIC STRUCTURE AND
CHARGE-DENSITY-WAVE FORMATION IN TISE₂**

Below we present further details on the computational procedures, high-T phase crystal structure, phonon frequencies, PBE+U calculations, spin-orbit coupling and electronic structure compared to ARPES.

COMPUTATIONAL DETAILS

Results with PBE and PBE+U were obtained with Quantum ESPRESSO [37] and results with HSE06 with VASP [39, 40] within the projector-augmented-wave (PAW) method. [41] A plane-wave cut-off of 320 eV was used and semi-core electrons were included in the Ti PAW potential. Results were converged with a $24 \times 24 \times 12$ k -point mesh in the high-T cell. For most calculations presented in the manuscript we used the all-electron CRYSTAL code [38] with an adapted molecular def2-TZVP basis set for solid state calculations. The results for the energy gain in HSE06 was within 1 meV/supercell in agreement between VASP and CRYSTAL (see Fig. 6 below).

HIGH-T PHASE CRYSTAL STRUCTURE

In Table I we present the experimental and theoretical lattice parameters and Se- z -positions of the high-T phase structure. The parameter a is the in-plane hexagonal lattice constant, c is the distance between layers and h is the distance between the Ti and Se layers. The hybrid functionals in combination with a simple Grimme D2[28] van der Waals correction give lattice parameters in good agreement with experiments. In our calculations we have, however, consistently used the experimental lattice parameters but relaxed atomic positions. Only the energy gain curves in Fig. 1 (b) of the manuscript were obtained with fixed Se- z -positions and fixed $\delta\text{Ti}/\delta\text{Se}(= 3)$ ratio. At the minimum the atomic positions were again relaxed as described in the manuscript. In Fig. 1 we show the in-plane crystal structure in the high -and low-T phases. Big blue dots signifies Ti atoms and small green dots Se atoms. A dot on the Se atom indicates that the atom is on the opposite side of the Ti layer as compared to the Se atom without the dot. We have also replotted in a larger scale the p , d and $p - d$ -hybridized orbitals of Fig. 3 (c) in the manuscript.

Table I. Lattice parameters are calculated within PBE, HSE06 and HSE(17,0). The van der Waals forces are accounted for via a Grimme D2[28] correction.

	Exp.[29]	PBE	HSE06	HSE(17,0)
$a(\text{\AA})$	3.540	3.519	3.528	3.531
$c(\text{\AA})$	6.007	6.130	6.104	6.113
$h(\text{\AA})$	1.532	1.555	1.522	1.527

PHONON FREQUENCIES IN THE HIGH-T PHASE

The phonon frequencies in the high-T phase are reported in Table II. In the high-T phase the phonons are measured at room temperature and thus cannot be calculated exactly within the harmonic approximation. Indeed, the two Raman active phonons at $200 \text{ cm}^{-1}(A_{1g})$ and at $136 \text{ cm}^{-1}(E_g)$ are overestimated by hybrid functionals. It is expected that thermal effects would soften these values, and this trend was seen in experiment at least for the E_g mode in the high-T phase.[47] On the contrary, the IR active mode around 140 cm^{-1} is underestimated, with both HSE06 and HSE(17,0). This mode belongs to the same phonon branch as the soft mode at L which drives the instability and should thus harden significantly with temperature. Such behaviour can also be seen in experiment.[44]

Table II. Calculated zone center phonon frequencies (cm^{-1}) for the high-T structure compared with Raman (R) and Infrared (I) experiments.

Symm.	Exp.	PBE	HSE06	HSE(17,0)
E_g (R)	136[36] (273 K) / 134[21] (300 K)	136.9	147.5	147.3
E_u (I)	143[45] (300 K) / 137[21] (300 K)	141.5	124.8	101.1
A_{1g} (R)	200[36] (273 K) / 194[21] (300 K)	195.6	209.5	207.9
A_{2u}	-	292.7	323.8	314.4

PHONON FREQUENCIES IN THE LOW-T PHASE

Tables III, IV and V report the computed Raman and infrared active frequencies in the CDW phase, comparing them to the peaks identified in several experimental spectra. They also contain an analysis of the CDW spectra in terms of back-folding of phonon modes from the Brillouin zone of the high-T phase. The q -points of the original lattice folded onto $\bar{\Gamma}$ in the supercell are Γ and A with weights 1, plus M and L with weights 3. By applying crystalline translations, all the phonon eigenvectors at $\bar{\Gamma}$ of the undistorted supercell are obtained from the phonon eigenvectors at the previously mentioned q -points of the unit cell. The degeneracy between frequencies at symmetry equivalent points is broken by the distortion, so that, e.g., the three degenerate modes from L_1 , L_2 and L_3 split into an E and an A representation.

We label $|\sigma_{\mathbf{q}}\rangle$ the phonon eigenvectors at $\bar{\Gamma}$ of the high-T phase. \mathbf{q} labels the q -point the mode is back-folded from. We then label $|\bar{\nu}\rangle$ the eigenvectors of the distorted low-T phase. We define the decomposition of a mode $|\bar{\nu}\rangle$ as the square overlap with the eigenvectors of the undistorted supercell $|\langle \bar{\nu} | \sigma_{\mathbf{q}} \rangle|^2$, and then sum over degenerate frequencies in the undistorted supercell. For any given $|\bar{\nu}\rangle$ we report in the tables the largest square overlaps as a function of σ (the ones larger than 10%), the frequency ω_{σ} and the point \mathbf{q} .

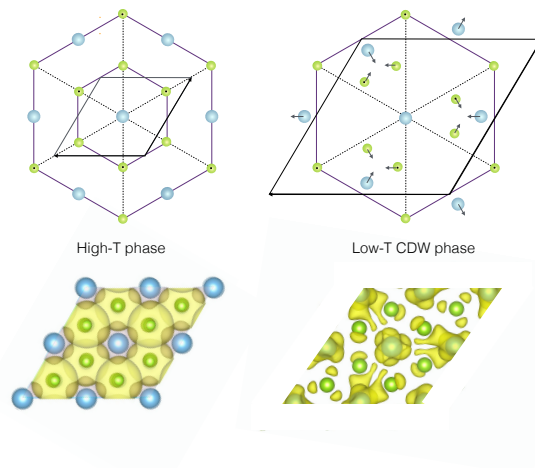


Figure 4. In-plane crystal structure of the high- and low-T phases and the corresponding p , d and $p-d$ hybridized orbitals that participate in the CDW transition.

Table III. Raman peaks identified in experimental spectra of the CDW phase (at 53 K and 11K) compared to computed Raman active frequencies (cm^{-1}). The point(s) \mathbf{q} in the Brillouin zone and the frequency(s) $\omega_{\text{undist.}}$ of the mode(s) of undistorted cell overlapping with the modes in the distorted cell are also reported, with the overlap percentage between parentheses. Only peaks identified as one phonon modes either in the experimental references or in this work are listed.

Symmetry	Exp.		Comment	Calc.		\mathbf{q}	$\omega_{\text{undist.}}$	
	53 K [21]	11K [36]		HSE(17,0)	PBE		HSE06	HSE06
E_g				30	31	A	28.3 (100)	
E_g	74	78	CDW	80.3	72.6	L	55.9	-126 (95)
E_g	93	94		94.4	97.0	L	93.7	94.7 (97)
A_{1g}	116	119	CDW	126	114	L	96.8	-126 (75) + 117 (17)
E_g	114	115		115	118	L	111	117 (100)
A_{1g}		115		114	119	L	112	117 (83) + -126 (16)
E_g	136	138		136,139	141,144	L	133 (41)+152 (41)	151 (50) +147 (35)
E_g	148		weak					
E_g				154	155	M+A	144	150 (53) + 133 (34)
E_g				154	157	$\Gamma + L$	148	147 (54) + 152 (39)
A_{1g}		151,158,163	weak					
A_{1g}	173	176		180	180	M	166	177.1 (94)
E_g				179	179	M+L+A	168	177 (72) + 205 (15) + 133 (10)
A_{1g}	187	195		200	202	M	187	204 (93)
E_g				201	203	M	189	204 (83) + 205 (12)
A_{1g}	204	206		215	214	Γ	199	210 (92)
E_g		212		217	215	L(80%) +M	202	207 (70) + 207 (12)
E_g	314	317		327	328	L	297	320 (99)

Table IV. Infrared phonons at obtained from reflectivity (ref.) and transmission (tr.) spectra. Peaks identified in infrared spectra of the CDW phase obtained from reflectivity (ref.) and transmission (tr.) experiments compared to computed infrared active frequencies of E_u symmetry. The point(s) \mathbf{q} in the Brillouin zone of the mode(s) of undistorted cell overlapping with the modes in the distorted cell are also reported.

Exp. ref.		Exp. tr.		Comment	Calc.			\mathbf{q}
18 K[45]	20 K[21]	28 K [44]	4 K [46]		HSE(17,0)	HSE06	PBE	
	42	40	37	weak				
	52	47	49	weak				
	64	64	64	weak				
	76	74	72	CDW	73.3	67.5	66	M
	90	88	100	weak	102	105	100	M
118.2	118	118	118	weak	119	123	115	M
139.5	137	139	140		137,138	141,143	132,137	Γ +L,A+M
151.3	152	152	153		152,155	154,156	143,150	M+A,L+ Γ
	162	166	164	weak				
171.9	175	176	173		176	177	167	L+M
	178		186	weak				
196.9	198	198	198		203	205	192	L+M
213.0		214	211		219	217	205	M+L
			222					
			230					
			280					
			315		330	333	305	M

Table V. Computed infrared active frequencies with the point(s) \mathbf{q} in the Brillouin zone and the frequency(s) $\omega_{\text{undist.}}$ of the mode(s) of undistorted cell overlapping with the modes in the distorted cell. The overlap percentage is reported between parentheses.

Symmetry	HSE(17,0)	PBE	HSE06	\mathbf{q}	$\omega_{\text{undist.}}$	HSE06
E_u	73.3	66.1	78.9	M	-100	(96)
A_{2u}	101	99.7	105	M	102	(92)
E_u	102	100	106	M	102	(96)
E_u	119	115	123	M	122	(99)
E_u	137	132	141	Γ +L	124 (60) + 152 (30)	
E_u	138	136	143	A+M	149 (60) + 147 (30)	
A_{2u}	143	137	150	L+M	152 (74) + 147 (25)	
A_{2u}	146	139	151	M+L	147 (71) + 152 (26)	
E_u	152	143	155	M+A	147 (62) + 149 (33)	
E_u	155	150	158	L+ Γ	152 (68) + 124 (24)	
E_u	176	167	177	L+M	176 (75) + 207 (12)	
E_u	203	192	206	L+M	207 (78) + 207 (16)	
A_{2u}	202	197	208	M	207 (98)	
E_u	219	205	218	M+L	207 (76) + 207 (15)	
A_{2u}	320	296	328	Γ +M	323 (69) + 329 (30)	
A_{2u}	326	301	332	M+ Γ	329 (69) + 323 (30)	
E_u	330	305	334	M	329 (99)	

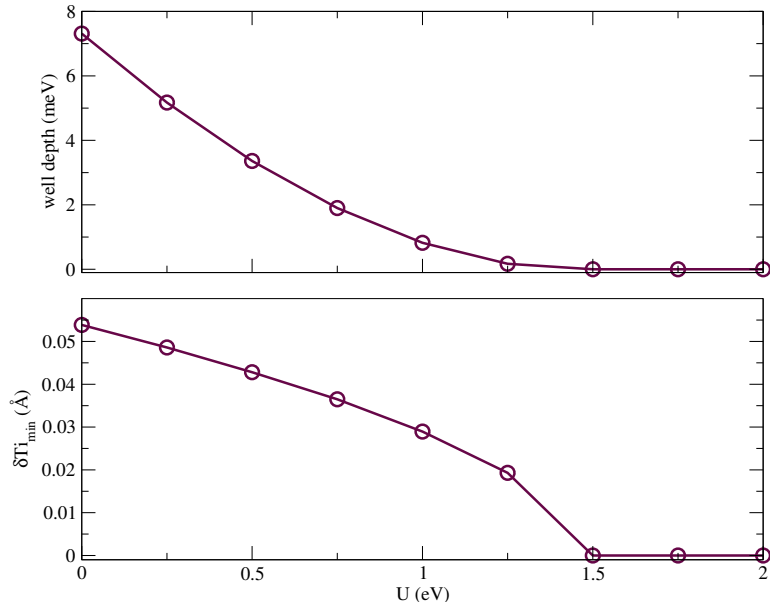


Figure 5. The upper panel shows the absolute energy gain or well-depth as a function of U within PBE+ U and the lower panel shows the corresponding displacement δTi_{\min} .

CDW INSTABILITY AS A FUNCTION OF U

In Fig. 5 we present the energy gain in the CDW distortion obtained with the PBE+ U method for values of U between 0 to 2 eV. We see that the energy gain reduces monotonically with U and vanishes at 1.5 eV. This can be compared to the LDA+ U result of $U=2.5$ eV in Ref. 24. The PBE+ U band-structure agrees well with HSE06 at $U=3.25$ eV. The corresponding value in LDA+ U is 3.5 eV.

SPIN-ORBIT COUPLING

The calculations presented in the main paper were obtained without spin-orbit coupling (SOC). We did, however, also perform calculations including SOC (using VASP since SOC is not an available option in CRYSTAL). We verified that SOC only added a minor quantitative correction and did not change the qualitative analysis. Including SOC increases the computational cost substantially and we could therefore only carry out a limited number of calculations. Furthermore, to make the calculations feasible we had to omit the $3p$ semi-core electrons in the Ti pseudo potential. This increases the energy gain but is not expected to change the effect of SOC, since SOC influences mainly the Se bands. The semi-core electrons are also not expected to largely influence the electron-phonon coupling (EPC) of the high-T phase. Indeed, we found a difference in the EPC of only 4%. In Fig. 6 we have summarised our analysis using HSE06. At large displacement δTi , the energy gain is around twice as large when omitting semi-core electrons. The effect is smaller, the smaller is the distortion, consistent with the fact that both the band structure and the EPC are very similar with and without semi-core electrons.

Including SOC we find only a very small change, the maximum being 2 meV at the minimum of the curve. At small distortion the difference is vanishingly small. The effect of SOC reduces the EPC in HSE06 from $19 \text{ eV}^2/\text{\AA}^2$ to $16 \text{ eV}^2/\text{\AA}^2$, which is compensated by the change in band structure. Apart from the indirect effect of SOC on the orbitals and the self-consistent potential there is a direct effect due to extra SOC terms in the Hamiltonian.[51] Since these terms are semi-local and density independent, we expect them to give only a small contribution to the non-local $p-d$ EPC and to be the same for all HSE functionals having the same band structure. The indirect effect is also expected to be small and similar for all HSE functionals. Indeed, similarly to HSE06, a reduction of approximately $3 \text{ eV}^2/\text{\AA}^2$ is found for HSE(30,0.3), which is accompanied by an identical change in band structure, and no difference in energy gain. We therefore expect that the relative EPC strengths with SOC and non local functionals are qualitatively

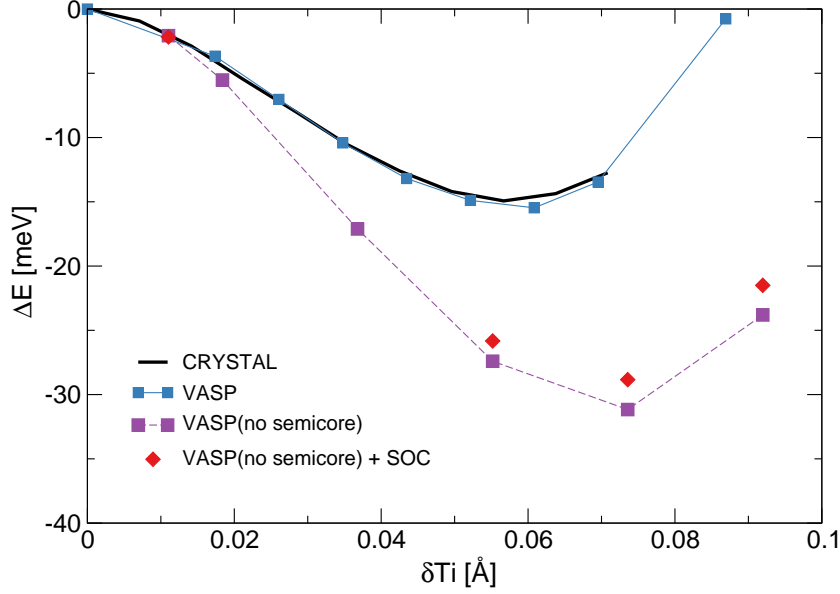


Figure 6. Energy gain within HSE06 calculated with CRYSTAL and VASP. We compare results with and without semi-core electrons in the Ti-PAW potential, and with and without SOC.

the same as those found without SOC.

ELECTRONIC STRUCTURE COMPARED TO ARPES

In order to compare the band structure with experiment it is important to take into account the Se- p band splitting around Γ in the high-T phase which is due to SOC. [26] In Fig. 7 we report calculated band structures in the high (a) -and low-T (b) phases superimposed on ARPES measurements by Rohwer et al.. [18] In the high-T phase we calculated the bands along $M' - \Gamma - M$ (black), $L' - \Gamma - L$ (orange) and along a line in between with $k_z = 0.33$ (red). The band dispersions are well-reproduced and the band overlap ($\Gamma - L$) is only slightly overestimated with HSE06. The bands in the CDW phase are calculated at the minimum of the curve in Fig. 1b of the manuscript and we note that band gap is indirect between Γ and A . The gaps in HSE06 and HSE(17,0) are 0.21 eV and 0.35 eV, respectively. Both are somewhat overestimated compared to the experimental value which has been estimated to 0.15 eV.

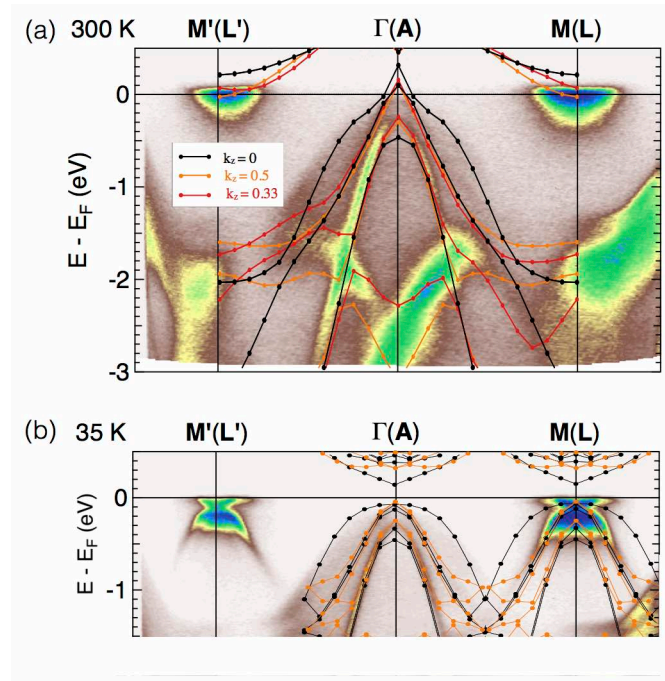


Figure 7. HSE06 electronic structure of the high (a) and low-T phases (b) compared to ARPES. k_z values are given in units of $2\pi/c$.